

Resonant power absorption in helicon plasma sources

Guangye Chen

*Department of Aerospace Engineering and Engineering Mechanics,
The University of Texas, Austin, Texas 78712*

Alexey V. Arefiev

Institute for Fusion Studies, The University of Texas, Austin, Texas 78712

Roger D. Bengtson

Physics Department, The University of Texas, Austin, Texas 78712

Boris N. Breizman

Institute for Fusion Studies, The University of Texas, Austin, Texas 78712

Charles A. Lee

Department of Electrical and Computer Engineering, The University of Texas, Austin, Texas 78712

Laxminarayan L. Raja

*Department of Aerospace Engineering and Engineering Mechanics,
The University of Texas, Austin, Texas 78712*

(Received 6 September 2006; accepted 8 November 2006; published online 26 December 2006)

Helicon discharges produce plasmas with a density gradient across the confining magnetic field. Such plasmas can create a radial potential well for nonaxisymmetric whistlers, allowing radially localized helicon (RLH) waves. This work presents new evidence that RLH waves play a significant role in helicon plasma sources. An experimentally measured plasma density profile in an argon helicon discharge is used to calculate the rf field structure. The calculations are performed using a two-dimensional field solver under the assumption that the density profile is axisymmetric. It is found that RLH waves with an azimuthal wave number $m=1$ form a standing wave structure in the axial direction and that the frequency of the RLH eigenmode is close to the driving frequency of the rf antenna. The calculated resonant power absorption, associated with the RLH eigenmode, accounts for most of the rf power deposited into the plasma in the experiment. © 2006 American Institute of Physics. [DOI: 10.1063/1.2402913]

I. INTRODUCTION

Helicon discharges use rf power to produce magnetized plasmas, operating at frequencies between the electron and ion gyrofrequency. Multiple applications of these discharges prompted experimental and theoretical research aimed at understanding the underlying physics.^{1–8} There are strong indications that the rf power deposition into the discharge involves excitation of an eigenmode that resonates with the rf antenna. A critical step is to identify the relevant eigenmode and to assess its role in the discharge.

Assuming that the eigenfrequency matches the rf antenna frequency, one can probe the eigenmode dispersion relation by varying discharge parameters. This was the basic concept of most previous experimental works designed to identify the eigenmode. In Ref. 1, the eigenmode was interpreted as a conventional whistler,⁹ based on the dependence of the average plasma density on the equilibrium magnetic field.

The whistler dispersion relation in a uniform plasma is given by⁹

$$\omega = \omega_{ce} \frac{c^2 k |k_{\parallel}|}{\omega_{pe}^2}, \quad (1)$$

where ω_{pe} and ω_{ce} are the plasma frequency and electron gyrofrequency, k is the absolute value of the wave vector,

and k_{\parallel} is the wave-vector component along the equilibrium magnetic field.

Equation (1) predicts that the density should be proportional to the magnetic field, which is consistent with the experimental data of Ref. 1. However, the assumption of $k=k_{\parallel}$ had to be made in Ref. 1 in order to reconcile Eq. (1) with the operational frequency. This assumption appears to be particularly vulnerable in the case of elongated modes with $k_{\parallel} \ll k$. The need for such an assumption indicates that Eq. (1) may not be applicable to the experimental conditions of Ref. 1.

Recently, a dedicated experiment was performed to unequivocally demonstrate that there is an eigenmode in the helicon discharge with a frequency close to the antenna frequency.⁸ The idea of the experiment was to keep all discharge parameters fixed while examining plasma response at various frequencies. This was achieved by using a high-power generator to create the discharge and a low-power variable frequency generator to excite test waves. The test waves were small perturbations to the overall rf field structure and, as a result, they did not affect the rf power deposition and the plasma density profile. A frequency scan of the plasma resistance revealed a sharp resonance associated with eigenmode excitation.

The observed resonance cannot be attributed to conven-

tional whistler waves, because Eq. (1) predicts a noticeably higher frequency than the frequency of the resonance. In the limit of $a \ll L$ (where a and L are the characteristic radius and length of the plasma), the lowest possible frequency in Eq. (1) corresponds to a mode with $k \approx \pi/a$ and $k_{\parallel} \approx \pi/L \ll k$. The experimental conditions of Ref. 8 are such that $a = 0.03$ m, $L \approx 0.30$ m, the equilibrium magnetic field is 627 G, and the characteristic plasma density is 10^{18} m⁻³. It then follows from Eq. (1) that the whistler eigenfrequency is at least $f \approx 65$ MHz, which is almost 5 times higher than the experimental resonance frequency of 13.56 MHz.

The discrepancy between the actual operational frequency of elongated helicon plasma sources and the whistler eigenfrequency appears to be a commonplace phenomenon. This discrepancy is also pertinent to Ref. 1. The measurements of the rf field structure in Ref. 1 show that $k_{\parallel} \ll k$, because the characteristic transverse scale of the rf field is 50 mm, whereas the characteristic longitudinal scale is 0.25 m. By setting $k = k_{\parallel}$ and $\omega \approx \omega_{ce} k_{\parallel}^2 c^2 / \omega_{pe}^2$, the authors of Ref. 1 underestimate the whistler eigenfrequency by a large factor of k/k_{\parallel} .

We conjecture that the cause of the described discrepancy is a significant plasma density gradient across the equilibrium magnetic field, which can dramatically modify both the whistler wave structure and its dispersion relation.¹⁰ Such a gradient is commonly observed in helicon sources when the guiding magnetic field is sufficiently strong.^{1,11–14} A radial density gradient in a plasma cylinder can create a potential well for nonaxisymmetric whistlers, allowing radially localized solutions with relatively low frequencies⁷ that we will refer to as radially localized helicon (RLH) waves. The dispersion relation for RLH waves is consistent with the experimental results reported in Refs. 1, 8, and 15–17, since the eigenmode frequency scales as $\omega \approx \omega_{ce} k_{\parallel}^2 c^2 / \omega_{pe}^2$.

In this paper, we present new theoretical and experimental evidence confirming that RLH waves can play a major role in helicon plasma sources. Our quantitative analysis is performed for a helicon plasma source similar to the one used in Ref. 8. We first demonstrate that there is a resonance close to the discharge driving frequency that is associated with the RLH eigenmode excitation. In order to do this, we have measured the plasma density profile in our helicon source. The knowledge of the density profile allows us to calculate the rf field structure. The calculations are performed with a two-dimensional (2D) field solver under the assumption that the density profile is axisymmetric, which is consistent with measurements. We have calculated the rf power absorption for frequencies close to the discharge driving frequency and we find that the rf power absorption has a resonance peak similar to the one described in Ref. 8. We perform a series of tests to relate the resonance to excitation of a *standing RLH wave* inside a cavity formed in the axial direction by the ideally conducting end walls of the source.

Our next step is to demonstrate that the eigenmode can actually account for most of the rf power deposited by the main generator. The knowledge of the electron collision frequency, which depends on gas density, is needed to compute the rf power absorption directly. However, the gas density is difficult to measure accurately in the experiment. We can

only specify the range for the collisional damping rate that allows for the experimentally measured power to be deposited into the plasma. An upper limit for the damping rate defines an upper limit for the gas pressure. We find that this limit is comparable to the measured fill pressure. Moreover, the measured damping rate in Ref. 8 is close to the calculated upper limit for the damping rate. These facts suggest that the discharge operates in a regime where the resonance is responsible for the rf power absorption by the plasma.

The rf field calculations show that the RLH mode is accompanied by electrostatic Trivelpiece-Gould (TG) waves.¹⁸ However, we find that for the experimental parameter range, most of the rf power absorption in the plasma volume is associated with the RLH mode. The electrostatic waves account for about 10% of the absorbed rf power, which is qualitatively different from the case of radially uniform plasma wherein TG waves are expected to play the dominant role in the power deposition.^{19–23}

It is appropriate to mention that the strong effect of plasma density gradient on helicon discharges has been observed in several previous numerical simulations.^{20,22,24–26} However, these observations have not been attributed to the existence of RLH modes, which appears to be a missing link in understanding power deposition mechanisms in the discharge. The need to find relevant mechanisms is apparent because the conventional helicon wave alone does not explain the observed power absorption.^{1,11} In an attempt to resolve this issue, collisionless heating by Landau damping has been studied as a possible cause of power deposition.^{2,21} Another candidate mechanism is associated with TG waves which may provide extra power deposition near the plasma edge. The physical picture changes when we recognize the existence of the RLH mode. In this paper, we show that the RLH wave produces stronger current along the magnetic field than the same-amplitude whistler wave in uniform plasma. The enhanced resistive heating caused by the RLH wave is able to explain most of the power deposition as well as the distribution of this power over the plasma volume.

The rest of the paper is organized as follows. Section II describes the experimental setup. In Sec. III, we introduce a finite difference scheme that is used to solve Maxwell's equations. Section IV presents simulation results for the experimental setup described in Sec. II, which includes rf field structure, power absorption density, and a power absorption scan. Finally, Sec. V gives some concluding remarks.

II. EXPERIMENT

The helicon source for this experiment (see Fig. 1) is identical to that in earlier experiments⁸ that presented experimental evidence for the existence of a resonant electromagnetic mode in a helicon plasma. A low-power variable frequency rf source was used to measure the plasma impedance of a helicon plasma created by a 1-kW rf driver at 13.56 MHz as a function of frequency in the range 11–16 MHz. The important experimental conclusions that can be drawn from these results are: (1) There exists a resonant electromagnetic mode in the helicon discharge in the frequency space around the driving frequency. (2) The reso-

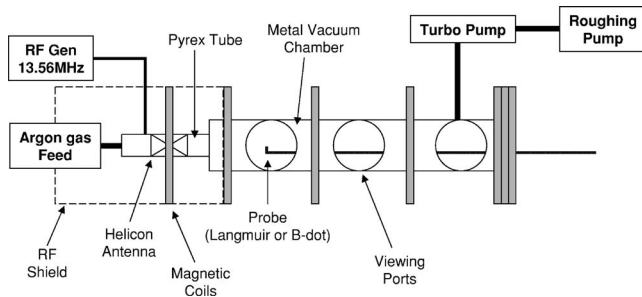


FIG. 1. Layout of the helicon experiment.

nant damping rate is much smaller than the driving frequency. The Q factor of the resonance is approximately 17.

We operate at similar conditions as earlier experiments,⁸ but did not reproduce the earlier plasma conditions. Plasma conditions are summarized in Table I. We use a Nagoya type III antenna with a 180° helical twist with a length of 0.15 m. The antenna was placed on a PyrexTM tube (Pyrex 7740) 60 mm in diameter, 0.3 m in length, with a wall thickness of 2 mm. The PyrexTM tube was connected to a cylindrical stainless vacuum chamber with an internal diameter of 95 mm and a total vessel length of 1.2 m from the gas inlet to the end of the vacuum chamber. Argon gas flowed through the PyrexTM tube and was pumped out by a turbo pump located at the downstream end of the vacuum chamber. Pressure was measured in the main vacuum chamber before the helicon was turned on. A magnetic field with a variation of less than 10% on axis is provided by seven magnetic coils.

The rf generator provides about 1100 W at 13.56 MHz and usually operates in a pulsed mode with a 20% duty cycle to allow for cooling of the matching network and antenna. For the plasma used in this work the RMS antenna current was 15 A measured by a current meter placed directly on the antenna.

The plasma density profile in the helicon was measured with a single rf compensated Langmuir probe²⁷ swept at 100 Hz. The dogleg probe was mounted on an axially moveable shaft at the edge of the plasma and rotated to different radial locations in the plasma. Locating the probe shaft at the lower density plasma edge reduced the disturbance to the plasma as compared to mounting the probe in a central (high-density) region. A boxcar averaged current versus voltage (I - V) curve is reduced from the 100-Hz voltage sweep. An electron temperature of 4.5 ± 0.3 eV was estimated from the I - V characteristics and was nearly constant axially and

TABLE I. Set of parameters for the helicon discharge under investigation.

RF power in	1 kW
RF frequency	13.56 MHz
Antenna current	15 A_{rms}
Neutral gas	Argon
Fill pressure	1 mTorr
Magnetic field	627 G
Electron temperature	4.5 eV
Maximum plasma density	$2.4 \times 10^{18} \text{ m}^{-3}$

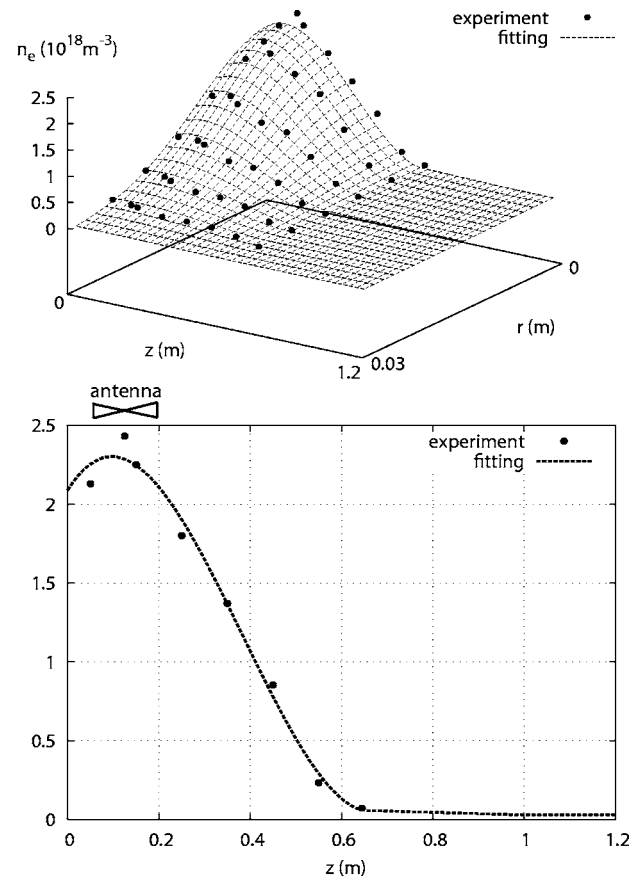


FIG. 2. Electron density profile in the helicon discharge. Top: Measured plasma density profile (black circles) is approximated by an analytical function (mesh) given by Eqs. (37) and (38). Bottom: On-axis plasma density profile, with experimentally measured values shown by black circles and the analytical fit shown by a dashed line.

radially, starting 5 mm from the wall. Rather than using the ion saturation current directly from the swept probe characteristics, we biased the probe to -24 V with respect to ground to drive the probe into ion saturation. The plasma potential was 22 V. The measured current was time averaged and converted to a 2D density profile using an electron temperature of 4.5 eV. Results are shown in Fig. 2. The relative measurement accuracy between density measurements when compared to each other is $\pm 4\%$. The uncertainty of each measurement on an absolute scale is $\pm 6\%$.

III. RF FIELD SOLVER

A. Wave equations

To simulate the experimental setup, we consider a cylindrical domain of radius L_r and length L_z , such that $r \in [0; L_r]$ and $z \in [0; L_z]$, where (r, ϕ, z) are cylindrical coordinates. The rf antenna and the plasma are located inside the cylinder and we assume that the surface of the cylinder is an ideal conductor. The equilibrium magnetic field \mathbf{B}_0 is uniform and it is directed along the axis of the cylinder, $\mathbf{B}_0 = B_0 \mathbf{e}_z$. The rf field is determined by the Maxwell's equations in frequency domain,

$$\nabla \times \mathbf{E} = \frac{i\omega}{c} \mathbf{B}, \quad (2)$$

$$\nabla \times \mathbf{B} = -\frac{i\omega}{c} \mathbf{D} + \frac{4\pi}{c} \mathbf{j}_a, \quad (3)$$

where \mathbf{E} and \mathbf{B} are the electric and magnetic fields, \mathbf{D} is the electric displacement vector, and \mathbf{j}_a is the antenna current density. The quantities \mathbf{D} and \mathbf{E} are linked to each other by a dielectric tensor $\varepsilon_{\alpha\beta}(r, z)$ that represents vacuum, glass, and cold plasma regions within the source. In the vacuum and glass regions, the dielectric tensor is $\varepsilon_{\alpha\beta} \equiv \varepsilon_*(r, z) \delta_{\alpha\beta}$, where $\delta_{\alpha\beta}$ is the Kronecker symbol and $\varepsilon_*(r, z)$ is a scalar. Specifically, $\varepsilon_* = 1$ in a vacuum region and $\varepsilon_* = \varepsilon_g$ in a glass region, where ε_g is the dielectric constant of glass. In the cold magnetized plasma, the dielectric tensor gives the following relations between \mathbf{D} and \mathbf{E} (Ref. 28):

$$D_r = \varepsilon E_r + ig E_\phi, \quad (4)$$

$$D_\phi = \varepsilon E_\phi - ig E_r, \quad (5)$$

$$D_z = \eta E_z, \quad (6)$$

where

$$\varepsilon = 1 - \sum_{\alpha} \frac{\omega + i\nu_{\alpha}}{\omega} \frac{\omega_{p\alpha}^2}{(\omega + i\nu_{\alpha})^2 - \omega_{c\alpha}^2}, \quad (7)$$

$$g = - \sum_{\alpha} \frac{\omega_{c\alpha}}{\omega} \frac{\omega_{p\alpha}^2}{(\omega + i\nu_{\alpha})^2 - \omega_{c\alpha}^2}, \quad (8)$$

$$\eta = 1 - \sum_{\alpha} \frac{\omega_{p\alpha}^2}{\omega(\omega + i\nu_{\alpha})}. \quad (9)$$

Here the subscript α labels particle species, namely electrons and ions; $\omega_{p\alpha} \equiv \sqrt{4\pi n_{\alpha} q_{\alpha}^2 / m_{\alpha}}$ is the plasma frequency, $\omega_{c\alpha} \equiv q_{\alpha} B_0 / m_{\alpha} c$ is the gyrofrequency, and ν_{α} is the collision frequency. In what follows, we assume that the plasma ions are singly charged, such that $q_i = -q_e = |e|$.

Assuming that the plasma density profile is axisymmetric, we use a Fourier expansion of \mathbf{E} , \mathbf{B} , and \mathbf{j}_a in azimuthal angle ϕ , and select a single Fourier harmonic that depends on ϕ as $e^{im\phi}$. Then the components of Eqs. (2) and (3) take the following form:

$$\frac{im}{r} E_z - \frac{\partial E_\phi}{\partial z} - \frac{i\omega}{c} B_r = 0, \quad (10)$$

$$\frac{\partial E_r}{\partial z} - \frac{\partial E_z}{\partial r} - \frac{i\omega}{c} B_\phi = 0, \quad (11)$$

$$\frac{1}{r} \frac{\partial(rE_\phi)}{\partial r} - \frac{im}{r} E_r - \frac{i\omega}{c} B_z = 0, \quad (12)$$

$$\frac{im}{r} B_z - \frac{\partial B_\phi}{\partial z} + \frac{i\omega}{c} D_r = \frac{4\pi}{c} j_{ar}, \quad (13)$$

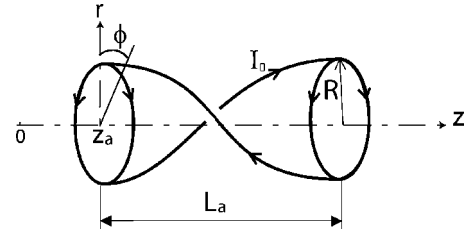


FIG. 3. Half-turn helical antenna. Here I_0 is the amplitude of the antenna current and z_a is the distance between the antenna and the end wall (located at $z=0$).

$$\frac{\partial B_r}{\partial z} - \frac{\partial B_z}{\partial r} + \frac{i\omega}{c} D_\phi = \frac{4\pi}{c} j_{a\phi}, \quad (14)$$

$$\frac{1}{r} \frac{\partial(rB_\phi)}{\partial r} - \frac{im}{r} B_r + \frac{i\omega}{c} D_z = \frac{4\pi}{c} j_{az}. \quad (15)$$

The boundary conditions require that the tangential components of \mathbf{E} vanish at the surface of the ideally conducting cylinder, i.e.,

$$E_\phi(L_r, z) = E_z(L_r, z) = 0, \quad (16)$$

$$E_r(r, 0) = E_\phi(r, 0) = 0, \quad (17)$$

$$E_r(r, L_z) = E_\phi(r, L_z) = 0. \quad (18)$$

Also, all field components must be regular at the axis as $r \rightarrow 0$.

In our calculations we consider a half-turn helical antenna shown in Fig. 3. We assume that the antenna current is divergence free, which eliminates capacitive coupling. Then the Fourier components of the antenna current density are given by

$$j_{ar} = 0, \quad (19)$$

$$j_{a\phi} = I_0 \frac{e^{im\pi} - 1}{2} \delta(r - R) \left(\frac{i}{m\pi} [\delta(z - z_a) + \delta(z - z_a - L_a)] + \frac{H(z - z_a)H(z_a + L_a - z)}{L_a} e^{-im\pi[1+(z-z_a)/L_a]} \right), \quad (20)$$

$$j_{az} = I_0 \frac{e^{-im\pi[1+(z-z_a)/L_a]} - 1}{\pi R} \frac{1 - e^{im\pi}}{2} \delta(r - R) \times H(z - z_a)H(z_a + L_a - z), \quad (21)$$

where I_0 is the amplitude of the current, L_a is the antenna length, z_a is the distance between the antenna and the end wall at $z=0$, and H is the Heaviside step function. Note that the antenna geometry selects only odd harmonic numbers m .

We use a finite difference method to solve Eqs. (10)–(15) directly as a set of first-order equations. It should be noted that this procedure differs from that of Ref. 29, where Eqs. (2) and (3) were first combined into a closed set of second-order equations for E_r , E_ϕ , and E_z .

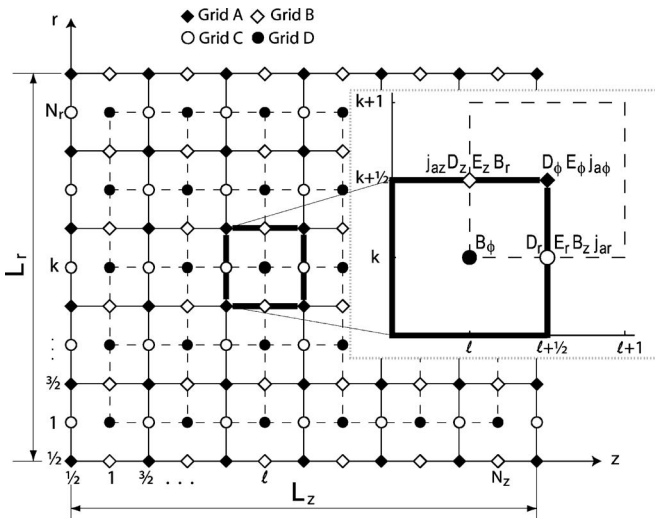


FIG. 4. Computational grid that consists of four staggered grids: grid A (black diamonds), grid B (open diamonds), grid C (open circles), and grid D (black circles).

B. Finite difference scheme

We introduce four staggered rectangular grids (A, B, C, and D) to discretize the fields in the rectangular computational domain with $r \in [0; L_r]$ and $z \in [0; L_z]$. Grid A consists of “half-integer” points with coordinates $(r_{k+1/2}, z_{l+1/2})$, where $k \in [0; N_r]$ and $l \in [0; N_z]$ are integer indexes. By definition, we have $r_{1/2}=0$, $r_{N_r+1/2}=L_r$, $z_{1/2}=0$, and $z_{N_z+1/2}=L_z$. The inner points of grid A can be distributed nonuniformly if needed to accommodate the source setup.

In addition, we introduce points with integer indexes,

$$r_k \equiv \frac{r_{k+1/2} + r_{k-1/2}}{2}, \quad (22)$$

$$z_l \equiv \frac{z_{l+1/2} + z_{l-1/2}}{2}. \quad (23)$$

We now define the grids B, C, and D as follows. Grid B consists of points with coordinates $(r_{k+1/2}, z_l)$, where $k \in [0; N_r]$ and $l \in [1; N_z]$. Grid C consists of points with coordinates $(r_k, z_{l+1/2})$, where $k \in [1; N_r]$ and $l \in [0; N_z]$. Grid D consists of points with coordinates (r_k, z_l) , where $k \in [1; N_r]$ and $l \in [1; N_z]$. We discretize \mathbf{E} , \mathbf{B} , \mathbf{D} , and \mathbf{j}_a as shown in Fig. 4. Namely, the quantities E_ϕ , D_ϕ , and $j_{a\phi}$ are defined on grid A; the quantities E_z , B_r , D_z , and j_{az} are defined on grid B; the quantities E_r , B_z , D_r , and j_{ar} are defined on grid C; and B_ϕ is defined on grid D.

The use of the staggered grids is motivated by the structure of Eqs. (10)–(15) (Ref. 30). For example, Eq. (10) involves B_r , E_ϕ , and E_z , with E_ϕ entering only the z derivative. Therefore, we discretize B_r and E_z on the same grid, and E_ϕ on a grid that is shifted in z with respect to it. We apply a similar approach to the remaining components of the Maxwell’s equations and the resulting finite difference equations are listed in the Appendix. Equations (A1) and (A6) approximate Eqs. (10) and (15) on grid B; Eq. (A2) approximates Eq. (11) on grid D; Eqs. (A3) and (A4) approximate Eqs.

(12) and (13) on grid C; and Eq. (A5) approximates Eq. (14) on grid A. Note that we write the finite difference equations only for *inner* points of the grids. The corresponding range of indexes for Eqs. (A1)–(A6) is specified in the Appendix.

1. Interpolation procedure

In a magnetized plasma, D_r depends on both E_r and E_ϕ . Components D_r and E_r are defined on grid C, whereas E_ϕ is defined on grid A. Therefore, discretization of Eq. (4) requires an interpolation procedure. We use two points of grid A, $(r_{k-1/2}, z_{l+1/2})$ and $(r_{k+1/2}, z_{l+1/2})$, that are radially adjacent to a point of grid C with coordinates $(r_k, z_{l+1/2})$ to write a discretized expression for the relation (4) at $(r_k, z_{l+1/2})$. In a similar way we write a discretized expression for the relation (5). As a result, Eqs. (4)–(6) translate into

$$D_r(r_k, z_{l+1/2}) \equiv [\varepsilon E_r](r_k, z_{l+1/2}) + \alpha_k^+ [igE_\phi](r_{k+1/2}, z_{l+1/2}) + \alpha_k^- [igE_\phi](r_{k-1/2}, z_{l+1/2}), \quad (24)$$

$$D_\phi(r_{k+1/2}, z_{l+1/2}) \equiv [\varepsilon E_\phi](r_{k+1/2}, z_{l+1/2}) - \beta_{k+1/2}^+ [igE_r](r_{k+1}, z_{l+1/2}) - \beta_{k+1/2}^- [igE_r](r_k, z_{l+1/2}), \quad (25)$$

$$D_z(r_{k+1/2}, z_l) \equiv [\eta E_z](r_{k+1/2}, z_l), \quad (26)$$

where α_k^\pm and $\beta_{k+1/2}^\pm$ are interpolation coefficients.

Our choice of α_k^\pm and $\beta_{k+1/2}^\pm$ reflects the following physics considerations. The rf electric field must satisfy the condition $(\nabla \cdot \mathbf{D})=0$, since we assume the antenna current to be divergence free, $(\nabla \cdot \mathbf{j}_a)=0$. We use Eqs. (4)–(6) to write $(\nabla \cdot \mathbf{D})=0$ as

$$\frac{1}{r} \frac{\partial}{\partial r} (r \varepsilon E_r) + \frac{i}{r} \frac{\partial}{\partial r} (r g E_\phi) + \frac{im}{r} \varepsilon E_\phi + \frac{m}{r} g E_r + \frac{\partial}{\partial z} (\eta E_z) = 0. \quad (27)$$

This condition is satisfied only approximately in the finite difference equations, with an accuracy dependent on the interpolation procedure. Discretization errors introduce fictitious external charge that needs to be minimized. The terms that are affected by the interpolation in Eq. (27) are only the terms that involve g . Discretization errors are enhanced in the region near the axis due to the $1/r$ factor. In this region, the g terms dominate in Eq. (27), because $\varepsilon/g \approx \omega/\omega_{ce}$. The interpolation is designed to achieve the best accuracy in calculating these terms.

In order to determine coefficients α_k^\pm , we consider the second term in Eq. (27). We discretize equation $(\nabla \cdot \mathbf{D})=0$ using the staggered grid discretization of \mathbf{D} the same way we discretized the Maxwell’s equations. We then use Eqs. (24)–(26) to express components of \mathbf{D} in terms of components of \mathbf{E} to find

$$\begin{aligned}
\left[\frac{1}{r} \frac{\partial}{\partial r} (rD_r) \right] (r_{k+1/2}, z_{l+1/2}) &\approx \frac{1}{r_{k+1/2}} \frac{r_{k+1} D_r(r_{k+1}, z_{l+1/2}) - r_k D_r(r_k, z_{l+1/2})}{r_{k+1} - r_k} \\
&= \frac{i}{r_{k+1/2}} \frac{\alpha_{k+1}^+ r_{k+1} [gE_\phi](r_{k+3/2}, z_{l+1/2}) + (\alpha_{k+1}^- r_{k+1} - \alpha_k^+ r_k) [gE_\phi](r_{k+1/2}, z_{l+1/2}) - \alpha_k^- r_k [gE_\phi](r_{k-1/2}, z_{l+1/2})}{r_{k+1} - r_k} \\
&\quad + \frac{1}{r_{k+1/2}} \frac{r_{k+1} [\varepsilon E_r](r_{k+1}, z_{l+1/2}) - r_k [\varepsilon E_r](r_k, z_{l+1/2})}{r_{k+1} - r_k}. \tag{28}
\end{aligned}$$

The combination that involves g is a finite difference representation of $(i/r)\partial(rgE_\phi)/\partial r$ in our scheme. The expression involves three different values of E_ϕ from three consecutive points of grid A.

On the other hand, one can discretize the radial derivative $(i/r)\partial(rgE_\phi)/\partial r$ at $(r_{k+1/2}, z_{l+1/2})$ using only the values of E_ϕ at $(r_{k+3/2}, z_{l+1/2})$ and $(r_{k-1/2}, z_{l+1/2})$,

$$\begin{aligned}
\frac{i}{r} \frac{\partial}{\partial r} (rgE_\phi)(r_{k+1/2}, z_{l+1/2}) \\
\approx \frac{i}{r_{k+1/2}} \frac{[rgE_\phi](r_{k+3/2}, z_{l+1/2}) - [rgE_\phi](r_{k-1/2}, z_{l+1/2})}{r_{k+3/2} - r_{k-1/2}}. \tag{29}
\end{aligned}$$

The advantage of this discretization is that a relative error for a *radially uniform* grid is of the order of h^2/λ^2 , where h is the step size and λ is the characteristic scale length of E_ϕ . The discretization that uses two adjacent grid points has a bigger relative error that can be estimated as h/λ . We choose α_k^\pm such that the combination involving g in Eq. (28) matches that in Eq. (29). Taking into account Eqs. (22) and (23), we find that the corresponding values of α_k^+ and α_k^- are

$$\alpha_k^+ = \frac{r_{k+1/2}}{2r_k}, \quad \alpha_k^- = \frac{r_{k-1/2}}{2r_k}. \tag{30}$$

Finally, we need to find coefficients $\beta_{k+1/2}^\pm$ such that the gE_r term in Eq. (27) has the same accuracy as the gE_ϕ term in the case of a uniform grid, i.e., the corresponding relative error must be h^2/λ^2 . This accuracy is achieved by a straightforward linear interpolation of gE_r in Eq. (5), because the term under consideration does not involve differentiation. We use the values of gE_r at $(r_{k+1}, z_{l+1/2})$ and $(r_k, z_{l+1/2})$ to evaluate gE_r at $(r_{k+1/2}, z_{l+1/2})$. This procedure yields the following interpolation coefficients in Eq. (25):

$$\beta_{k+1/2}^+ = \frac{r_{k+1/2} - r_k}{r_{k+1} - r_k}, \quad \beta_{k+1/2}^- = \frac{r_{k+1} - r_{k+1/2}}{r_{k+1} - r_k}. \tag{31}$$

The interpolation scheme given by Eqs. (24)–(26), (30), and (31) allows us to control the accuracy with which the $(\nabla \cdot \mathbf{D})=0$ condition is satisfied in the finite difference equations. Specifically, the interpolation scheme ensures consistency of the finite difference wave equations (A1)–(A6) with the $(\nabla \cdot \mathbf{D})=0$ condition if a uniform radial grid is used near the axis. Indeed, any other choice of α_\pm would entail a relative error of the order of h/λ (rather than h^2/λ^2) in the discretized expression for the radial derivative $\partial(rgE_\phi)/\partial r$ near

the axis. The corresponding relative error in the discretized expression for $(1/r)\partial(rD_r)/\partial r$ would be h/r . This error would not vanish as $h \rightarrow 0$ at grid points near the axis where $r \approx h$. Physically, this nondisappearing error represents charge density that can cause spurious excitation of electrostatic waves near the axis. In contrast, our interpolation scheme ensures that the relative error vanishes at all grid points as $h \rightarrow 0$.

2. Boundary conditions

An important feature of the described numerical scheme is that index k in the finite difference equations runs from 1 to N_r for Eqs. (A2)–(A4) and from 1 to $N_r - 1$ for Eqs. (A1), (A5), and (A6). This means that only Eqs. (A2) and (A3) involve radial boundary conditions and these equations require only the values of E_ϕ and E_z at the boundary. In a similar way, index l runs from 1 to N_z for Eqs. (A1), (A2), and (A6) and from 1 to $N_z - 1$ for Eqs. (A3)–(A5). Thus only the values of E_r and E_ϕ are needed for the axial boundary conditions. Therefore, the discretized equations involve only tangential components of the electric field at the boundaries.

The boundary conditions at the ideally conducting walls specified by Eqs. (16)–(18) translate into

$$E_\phi(r_{N_r+1/2}, z_{l+1/2}) = E_z(r_{N_r+1/2}, z_l) = 0, \tag{32}$$

$$E_r(r_k, z_{1/2}) = E_\phi(r_{k+1/2}, z_{1/2}) = 0, \tag{33}$$

$$E_r(r_k, z_{N_z+1/2}) = E_\phi(r_{k+1/2}, z_{N_z+1/2}) = 0. \tag{34}$$

We seek a solution that is regular at the axis, which requires that the quantity rE_ϕ vanish at the axis. Also, for $m \neq 0$, E_z must vanish at the axis, so that

$$r_{1/2} E_\phi(r_{1/2}, z_l) = 0, \tag{35}$$

$$E_z(r_{1/2}, z_l) = 0. \tag{36}$$

Equations (35) and (36) complete the set of boundary conditions.

The finite difference equations (A1)–(A6) with conditions (32)–(36) comprise a system of $6N_r N_z - 3(N_r + N_z) + 1$ linear equations. We use the ‘‘Portable, Extensible Toolkit for Scientific Computation’’ (PETSc) (Ref. 31) to solve this linear system. In a typical calculation, the number of grid points in the radial direction is 300 and the number of grid points in

the axial direction is 160. We have verified the convergence of the solution by doubling the number of the grid points in both directions.

IV. SIMULATION RESULTS

In this section we numerically examine plasma response as a function of frequency and demonstrate that there is a plasma eigenmode with an eigenfrequency close to the discharge driving frequency. This eigenmode can account for most of the rf power absorbed by the plasma. To simulate the experimental setup, we use a computational domain shown in Fig. 5 with a uniform equilibrium magnetic field of 627 G and a somewhat simplified geometry of the rf shield and the vacuum chamber. The rf shield and the vacuum chamber are modeled by an ideally conducting chamber (see Fig. 5). The measured plasma density profile is approximated by an analytical function shown in Fig. 2, which is used to evaluate the dielectric tensor $\varepsilon_{\alpha\beta}$. The explicit form of this function is

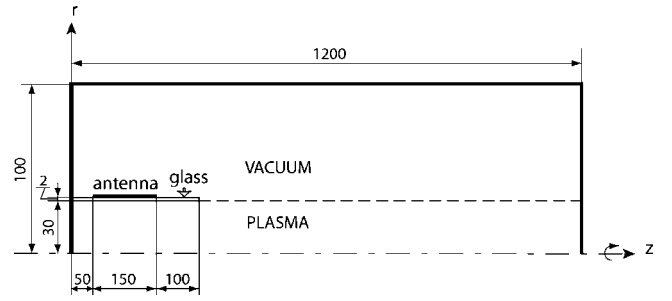


FIG. 5. Computational domain used to simulate the experimental setup shown in Fig. 1. Here all dimensions are given in millimeters.

$$n(r, z) = N \left(\frac{z}{L_z} \right) \exp \left[-3.8 \left(\frac{r}{R_p} \right)^2 \right] 10^{18} \text{ m}^{-3}, \quad (37)$$

where $L_z = 1.2$ m is the length of the ideally conducting cavity, $R_p = 0.03$ m is the radius of the plasma, and the function N is defined as

$$N(\xi) \equiv \begin{cases} 2.089 + 5.53\xi - 39.114\xi^2 + 39.152\xi^3 + 2.6\xi^4, & \xi \in [0, 0.5375]; \\ 0.1106 - 0.098\xi, & \xi \in [0.5375, 0.833]; \\ 0.0289, & \xi \in [0.833, 1]; \end{cases} \quad (38)$$

where $\xi \equiv z/L_z$.

In order to perform a frequency scan of the plasma power absorption, we select an azimuthal wave number m and specify electron collision frequency $\nu_e(r, z)$. Using the field solver from Sec. III, we calculate the m -th Fourier component of the electric field, $\mathbf{E}(m, r, z)$, and then compute the resultant time-averaged power absorption density

$$Q_m(r, z) = -\frac{i\omega}{16\pi} (\varepsilon_{\alpha\beta} - \varepsilon_{\beta\alpha}^*) E_\alpha^*(m, r, z) E_\beta(m, r, z), \quad (39)$$

where the asterisk denotes the complex conjugate. We integrate $Q_m(r, z)$ over the entire plasma volume to find the rf power, P_m , absorbed by the plasma. Repeating this procedure for a range of antenna frequencies ω yields a frequency scan of power absorption, $P_m(\omega)$, for the selected value of m and fixed discharge parameters. The total rf power absorbed by the plasma at a given frequency is given by a sum over all harmonics, $P(\omega) = \sum P_m(\omega)$.

We have performed power absorption scans for $m = \pm 1, \pm 3, \pm 5$ and we find that the power absorption for $m = 1$, shown in Fig. 6 (top) for two different choices of $\nu_e(r, z)$, exceeds the power absorption for the other harmonics over the same frequency range by more than an order of magnitude, such that $P(\omega) \approx P_1(\omega)$. For comparison, Fig. 6 (bottom) shows power absorption scans for $m = -1$ and $m = 3$. A robust feature of the power absorption scans in Fig. 6 (top) is

a well-pronounced resonance peak near the discharge driving frequency $f_0 = 13.56$ MHz. The location of the peak, f_R , changes slightly with variations of $n(r, z)$ within the experimental error bars. Specifically, we find that $f_R = 13.54$ MHz ($\pm 3\%$) for density variations of $\pm 6\%$. Power absorption scans for different values of electron collision frequency indicate that the width of the peak decreases with ν_e , whereas the height of the peak increases with ν_e . This feature is illustrated in Fig. 6 (top), where the dashed line corresponds to a lower collision frequency than that in the scan shown by a solid line.

We relate the resonance peak in our calculations to the experimentally measured resonance peak from Ref. 8, where the experimental setup and conditions were similar. In Ref. 8, the experimentally measured damping rate is $\gamma_{\text{exp}} = 2.4 \times 10^6 \text{ sec}^{-1}$ which is only 3% of the resonance frequency. Note that this value of γ is consistent with the value of the damping rate given in Ref. 8, because the damping rate in Table II of Ref. 8 is defined as $\gamma/2\pi$. The error bars in the plasma density measurements in our experiment cause an uncertainty in the value of the resonance frequency of the order of $\pm 3\%$. This creates a significant uncertainty in the calculations of the power deposition at a given frequency. Yet the power scan for a given damping rate (given collision frequency) gives a robust upper boundary for the power absorption, which is the height of the resonance peak.

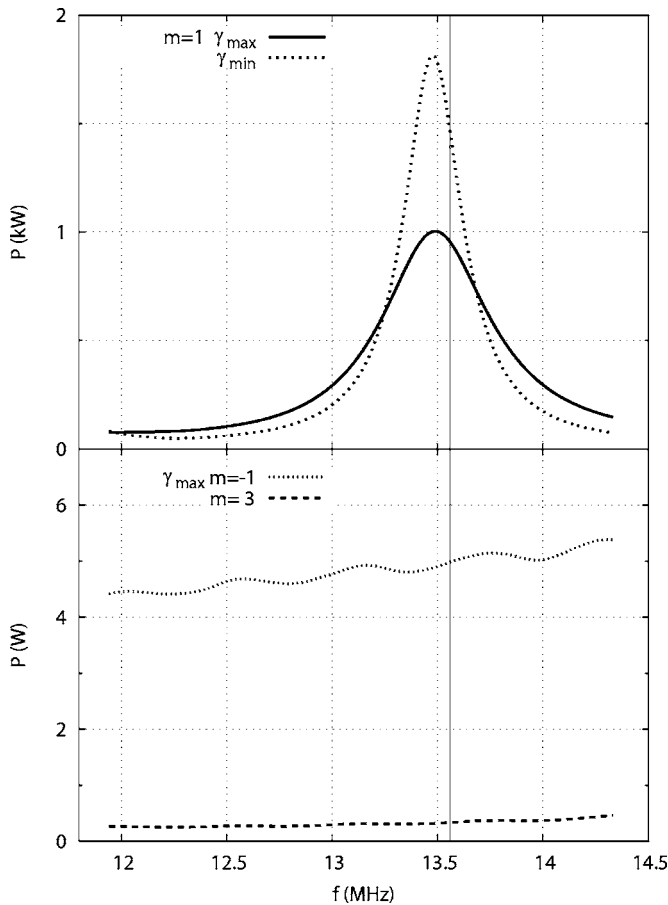


FIG. 6. Frequency scans of the rf power absorption. Top: Scans for $m=1$ with the maximum (γ_{\max}) and minimum (γ_{\min}) allowable damping rates. Bottom: Scans for $m=-1$ and $m=3$ with a damping rate γ_{\max} . The vertical line marks the driving frequency of the discharge. Note that the power is given in kilowatts on the top graph and in watts on the bottom graph.

We know from our measurements that the power provided by the generator is around 1 kW. Clearly, the resonance may be responsible for the power deposition into the plasma only if the height of the resonance peak is above 1 kW. The maximum power absorption in the resonance depends on a corresponding damping rate γ , which in turn depends on ν_e . The electron collision frequency is a sum of electron-neutral (ν_{en}) and electron-ion (ν_{ei}) collision frequencies, $\nu_e \equiv \nu_{en} + \nu_{ei}$, so that ν_e is always greater than ν_{ei} . We thus observe that by taking $\nu_e = \nu_{ei}$ we can obtain a lower limit for γ and an upper limit for the power deposition in the resonance.

We assume that plasma electrons have a Maxwellian distribution function with a spatially uniform experimentally measured temperature $T_e \approx 4.5$ eV. The electron-ion Coulomb collision frequency is given by $\nu_{ei} = 2.91 \times 10^{-12} n T_e^{-3/2} \ln \Lambda$ (Ref. 32), where T_e and n are expressed in eV and m^{-3} , respectively. The Coulomb logarithm is taken to be $\ln \Lambda = 12$. The power scan for $\nu_e = \nu_{ei}$ is shown in Fig. 6 by a dashed line. The corresponding lower limit for the damping rate is $\gamma_{\min} = 1.06 \times 10^6 \text{ sec}^{-1}$, which gives a 1.8-kW upper limit for the power deposition.

The requirement that the height of the peak must be at least 1 kW sets up an upper limit for the damping rate. The

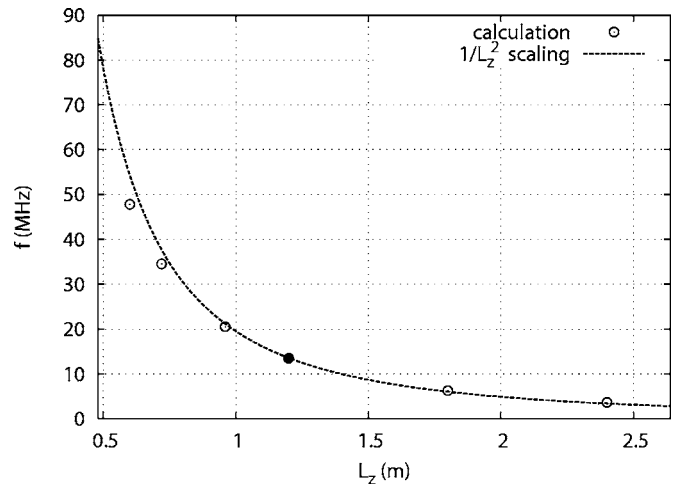


FIG. 7. Computed scaling of the RLH eigenfrequency for $m=1$ with the length of the source L_z (open circles). The eigenfrequency for the experimental density profile is shown by black circles. The dashed line shows a $1/L_z^2$ scaling that corresponds to the dispersion relation of RLH eigenmodes derived in Ref. 7.

power scan with a 1-kW peak is shown in Fig. 6 by a solid line. We adjust the electron collision frequency via adjusting the ambient gas density to make the height of the peak equal to 1 kW. The electron-neutral collision frequency is given by $\nu_{en} = n_g \langle \sigma_m v \rangle$, where n_g is the ambient gas density and σ_m is the elastic momentum transfer cross section.³³ The angular brackets in this expression stand for the averaging over the electron distribution function. We assume that the ambient gas density is uniform throughout the discharge and we find that an upper limit for the damping rate is $\gamma_{\max} = 2.01 \times 10^6 \text{ sec}^{-1}$. For a higher damping rate the power balance would not be satisfied.

The electron collision frequency is not directly known from the experiment, because it depends on the ambient gas density that we cannot accurately measure. We can only specify the range for the damping rate γ that allows for 1 kW of power to be deposited into the plasma. The gas pressure that corresponds to γ_{\max} is the upper limit for the gas pressure in the discharge. We find that this limit (0.45 mTorr) is comparable to the fill pressure before the plasma turns on (1 mTorr). Moreover, the damping rate $\gamma_{\text{exp}} = 2.4 \times 10^6 \text{ sec}^{-1}$ ($\pm 20\%$) that was experimentally measured in Ref. 8 is close to γ_{\max} . These facts signify that the discharge operates in a regime where the resonance is responsible for the rf power absorption by the plasma.

Next, we examine the dispersion relation for the eigenmode associated with the resonance. Figure 7 shows how the resonance frequency changes when we rescale the axial dimensions of the plasma, rf antenna, and computational domain by the same factor. The resonance frequency scales as $1/L_z^2$, which is in agreement with the dispersion relation of RLH eigenmodes.⁷ Indeed, the RLH dispersion relation in an axially uniform plasma predicts that $\omega \propto k_{\parallel}^2$, where k_{\parallel} is the axial component of the wave vector. On the other hand, the whistler dispersion relation in a uniform plasma⁹ predicts that $\omega \propto k_{\parallel}$ for modes with $k_{\parallel} \ll k$, which would correspond to a $1/L_z$ scaling. We also note that RLH modes require the sign

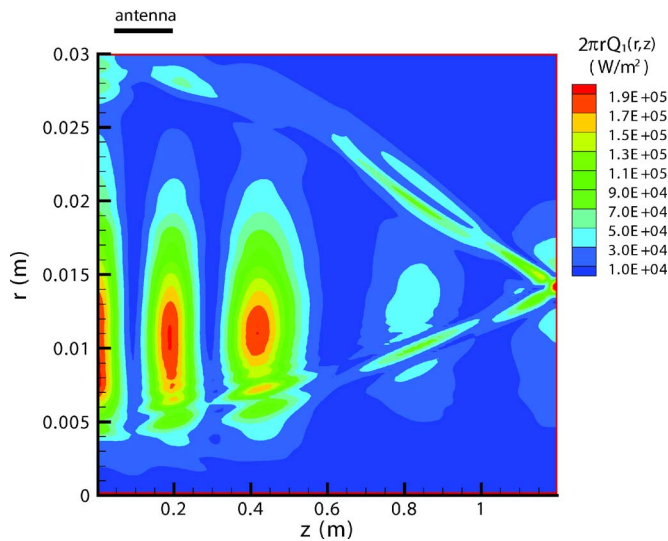


FIG. 8. (Color online) Contour plot of power absorption, $2\pi rQ_1(r,z)$, for $f=13.56$ MHz, $m=1$, and $\gamma=\gamma_{\max}=2\times 10^6$ sec $^{-1}$.

of m to be positive in our configuration, which explains the absence of a resonance peak for $m=-1$ in our calculations. We thus conclude that the resonance peak in Fig. 6 should be interpreted as an RLH eigenmode.

The rf power absorption density $Q_1(r,z)$ calculated for $f_0=13.56$ MHz and $\gamma=\gamma_{\max}$ is shown in Fig. 8. Most of the power is absorbed by the electrons in the bulk of the plasma, with 73% of the total power absorbed at $r<25$ mm and $z<0.6$ m. The plot of $Q_1(r,z)$ exhibits a quasiperiodic structure along z and an additional narrow elongated structure that starts under the antenna.

The quasiperiodic peaks of the power absorption in the axial direction are produced by the RLH eigenmode. The ideally conducting walls of the source form a cavity for the eigenmode in the axial direction. The observed resonance corresponds to a standing wave structure along z and, as a result, the plot of $Q_1(r,z)$ exhibits a sequence of peaks in the z direction.

The collisional power dissipation in the RLH mode is associated with the axial component of the electron current.³⁴ This component is greatly enhanced in the region with strong radial nonuniformity. Indeed, a nonaxisymmetric $m=1$ mode produces a Hall current that has a radial component. In a region with a radial density gradient, the radial Hall current must be accompanied by strong longitudinal current to keep the divergence of the total plasma current equal to zero and prevent charge separation. The enhancement of the axial electron current is the reason for radial localization of the rf power absorption in the region with strong radial nonuniformity.

The narrow elongated structure in the power absorption in Fig. 8 is associated with excitation of electrostatic TG waves.¹⁸ The TG waves are excited due to mode coupling, which is most pronounced at the plasma edge, where the radial Hall current from the RLH wave produces a surface charge.

The TG waves differ significantly from the RLH mode in their spatial structure. Figure 9 shows the radial structure

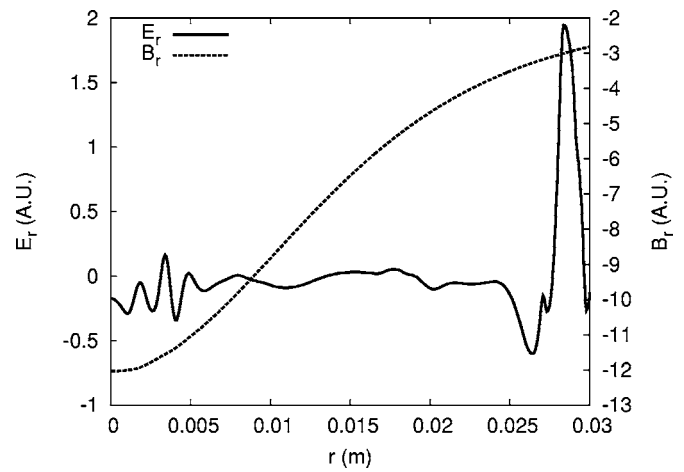


FIG. 9. Radial field structure at $z=0.15$ m. The small scale oscillations in E_r represent TG waves. The large scale structure in B_r represents the RLH eigenmode.

of rf field at $z=0.15$ m in the power absorption plot of Fig. 8. The radial electric field has two distinct spatial scales, with well-pronounced short scale oscillations. However, the short scale oscillations are not present in the rf magnetic field, which suggests that the short scales are associated with electrostatic TG waves,¹⁸ whereas the large scales are associated with the RLH eigenmode.

The wave vector of the TG waves is directed almost radially, since the corresponding characteristic radial scale length is much shorter than that of the RLH eigenmode. The corresponding group velocity of the TG waves is almost parallel to the confining magnetic field. The angle between the group velocity and the magnetic field is close to ω/ω_{ce} in the case of uniform plasma. The radial density gradient alters this angle, as can be seen from Fig. 8, as well as from a modified wave equation for the TG waves derived in Ref. 7.

The excited TG waves propagate away from the antenna along the plasma. They undergo reflection from the end wall at $z=L_z$ (see Fig. 8). The damping rate for these waves is much greater than that for the RLH mode, so that the TG waves decay on their way to the other end wall at $z=0$.

It is clear from Fig. 8 that the power absorption associated with the RLH eigenmode is much greater than the power absorption associated with the TG waves, which makes the RLH eigenmode the dominant factor in rf power deposition.

V. DISCUSSION AND CONCLUDING REMARKS

We have demonstrated that the helicon discharge in our experiment operates via excitation of a standing RLH wave. The standing wave is an eigenmode of a cavity formed in the axial direction by the ideally conducting end walls of the source. The eigenmode is weakly damped and, as a result, it produces a sharp resonance in the rf power absorption close to the discharge driving frequency. The resonant absorption allows for the eigenmode to account for most of the rf power deposited by the generator into the plasma.

The group velocity of RLH waves along the magnetic-field lines is $2\omega/k_{\parallel}$, where k_{\parallel} is the axial component of the

wave vector. An RLH wave with a damping rate γ travels a distance $\ell_v \equiv 2\omega/(\gamma k_{\parallel})$ before its amplitude decreases significantly. We have found from our calculations that an upper limit for the damping rate is $\gamma_{\max} = 2 \times 10^6 \text{ sec}^{-1}$ and the characteristic value of the axial component of the wave vector is $k_{\parallel} \approx 16 \text{ m}^{-1}$. The corresponding absorption length for the RLH wave is $\ell_v \approx 5 \text{ m}$. This length is much greater than the length of the cavity, which allows the RLH wave to form a standing wave structure with a sharp resonance response.

Helicon sources with a higher damping rate are expected to operate in a different regime if the plasma length exceeds the wave absorption length. For example, the helicon source described in Ref. 35 is longer than our source and the electron collision frequency is higher because the plasma density and the gas pressure are higher. In this case, waves excited by the antenna damp before they reach the end wall. As a result, the discharge cannot support a resonant eigenmode. It must be pointed out that several waves with comparable amplitudes can be simultaneously excited by the antenna in this nonresonant regime. These waves are not standing waves, but they can still produce an interference pattern similar to the standing wave pattern (see Ref. 36).

Finally, we note that the density gradient has a significant impact on the power absorption in the bulk of the plasma even in the absence of a resonance in the rf power absorption. For example, our calculations for the helicon source from Ref. 35 indicate that the power absorption in the bulk increases by more than a factor of 5 in the presence of the radial density gradient compared to the case when the density is radially uniform. Approximately 60% of the calculated total power is absorbed in the bulk for the experimentally measured density profile.

ACKNOWLEDGMENTS

This work was supported by AdAstra Rocket Company and by U.S. Department of Energy Contract No. DE-FG02-04ER54742.

APPENDIX: FINITE DIFFERENCE EQUATIONS

On the staggered grid, finite difference equations corresponding to the wave equations (10)–(15) have the following form:

$$\frac{im}{r_{k+1/2}} E_z(r_{k+1/2}, z_l) - \frac{E_{\phi}(r_{k+1/2}, z_{l+1/2}) - E_{\phi}(r_{k+1/2}, z_{l-1/2})}{z_{l+1/2} - z_{l-1/2}} - \frac{i\omega}{c} B_r(r_{k+1/2}, z_l) = 0, \quad (\text{A1})$$

$$\frac{E_r(r_k, z_{l+1/2}) - E_r(r_k, z_{l-1/2})}{z_{l+1/2} - z_{l-1/2}} - \frac{E_z(r_{k+1/2}, z_l) - E_z(r_{k-1/2}, z_l)}{r_{k+1/2} - r_{k-1/2}} - \frac{i\omega}{c} B_{\phi}(r_k, z_l) = 0, \quad (\text{A2})$$

$$\frac{1}{r_k} \frac{r_{k+1/2} E_{\phi}(r_{k+1/2}, z_{l+1/2}) - r_{k-1/2} E_{\phi}(r_{k-1/2}, z_{l+1/2})}{r_{k+1/2} - r_{k-1/2}} - \frac{im}{r_k} E_r(r_k, z_{l+1/2}) - \frac{i\omega}{c} B_z(r_k, z_{l+1/2}) = 0, \quad (\text{A3})$$

$$\frac{im}{r_k} B_z(r_k, z_{l+1/2}) - \frac{B_{\phi}(r_k, z_{l+1}) - B_{\phi}(r_k, z_l)}{z_{l+1} - z_l} + \frac{i\omega}{c} D_r(r_k, z_{l+1/2}) = \frac{4\pi}{c} j_{ar}(r_k, z_{l+1/2}), \quad (\text{A4})$$

$$\frac{B_r(r_{k+1/2}, z_{l+1}) - B_r(r_{k+1/2}, z_l)}{z_{l+1} - z_l} - \frac{B_z(r_{k+1}, z_{l+1/2}) - B_z(r_k, z_{l+1/2})}{r_{k+1} - r_k} + \frac{i\omega}{c} D_{\phi}(r_{k+1/2}, z_{l+1/2}) = \frac{4\pi}{c} j_{a\phi}(r_{k+1/2}, z_{l+1/2}), \quad (\text{A5})$$

$$\frac{1}{r_{k+1/2}} \frac{r_{k+1} B_{\phi}(r_{k+1}, z_l) - r_k B_{\phi}(r_k, z_l)}{r_{k+1} - r_k} - \frac{im}{r_{k+1/2}} B_r(r_{k+1/2}, z_l) + \frac{i\omega}{c} D_z(r_{k+1/2}, z_l) = \frac{4\pi}{c} j_{az}(r_{k+1/2}, z_l). \quad (\text{A6})$$

Index k runs from 1 to N_r in Eqs. (A2)–(A4) and from 1 to $N_r - 1$ in Eqs. (A1), (A5), and (A6). Index l runs from 1 to N_z in Eqs. (A1), (A2), and (A6) and from 1 to $N_z - 1$ in Eqs. (A3)–(A5).

In these equations, components of the electric displacement \mathbf{D} in a cold magnetized plasma are given by

$$D_r(r_k, z_{l+1/2}) \equiv \varepsilon(r_k, z_{l+1/2}) E_r(r_k, z_{l+1/2}) + \frac{i}{2r_k} [r_{k+1/2} g(r_{k+1/2}, z_{l+1/2}) E_{\phi}(r_{k+1/2}, z_{l+1/2}) + r_{k-1/2} g(r_{k-1/2}, z_{l+1/2}) E_{\phi}(r_{k-1/2}, z_{l+1/2})], \quad (\text{A7})$$

$$D_{\phi}(r_{k+1/2}, z_{l+1/2}) \equiv \varepsilon(r_{k+1/2}, z_{l+1/2}) E_{\phi}(r_{k+1/2}, z_{l+1/2}) - ig(r_{k+1}, z_{l+1/2}) E_r(r_{k+1}, z_{l+1/2}) \frac{r_{k+1/2} - r_k}{r_{k+1} - r_k} - ig(r_k, z_{l+1/2}) E_r(r_k, z_{l+1/2}) \frac{r_{k+1} - r_{k+1/2}}{r_{k+1} - r_k}, \quad (\text{A8})$$

$$D_z(r_{k+1/2}, z_l) \equiv \eta(r_{k+1/2}, z_l) E_z(r_{k+1/2}, z_l). \quad (\text{A9})$$

In a vacuum region, we put $\varepsilon = \eta = 1$ and $g = 0$ in Eqs. (A7)–(A9). In a glass region, we put $\varepsilon = \eta = 5.0$ [which is the value of a dielectric constant for Pyrex 7740 (Ref. 37)] and $g = 0$ in Eqs. (A7)–(A9).

We implement the half-turn helical antenna specified by Eqs. (19)–(21) using the following procedure. In order to avoid sharp gradients in the antenna current, we approximate j_{az} from Eq. (21) by

$$j_{az} = \frac{I_0 G(r)}{2\pi R} \frac{1 - e^{im\pi}}{2} \begin{cases} \left[\cos\left(\pi \frac{z - z_a + \Delta_z}{\Delta_z}\right) - 1 \right], & z \in [z_a - \Delta_z, z_a] \\ 2 \exp\left(i\pi m \frac{z_a - L_a - z}{L_a}\right), & z \in [z_a, z_a + L_a] \\ \left[\cos\left(\pi \frac{z - z_a - L_a}{\Delta_z}\right) + 1 \right], & z \in [z_a + L_a, z_a + L_a + \Delta_z] \\ 0, & \text{otherwise} \end{cases}, \quad (\text{A10})$$

where

$$G(r) \equiv \frac{1}{\sqrt{2\pi}\Delta_r} \exp\left(-\frac{(r-R)^2}{2\Delta_r^2}\right) \quad (\text{A11})$$

and Δ_z and Δ_r are small parameters. The antenna current has only ϕ and z components, with $j_{a\phi}$ defined on grid A and j_{az} defined on grid B. We discretize j_{az} and then use a discretized condition $(\nabla \cdot \mathbf{j}_a) = 0$ to find $j_{a\phi}$. This procedure is designed to eliminate capacitive coupling for the discretized components of the antenna current.

Equation (A10) is equivalent to Eq. (21) in the limit of $\Delta_z \rightarrow 0$ and $\Delta_r \rightarrow 0$. In our calculations, we take $z_a = 0.055$ m, $\Delta_z = 0.01$ m, $L_a = 0.14$ m, $R = 0.033$ m, and $\Delta_r = 1.67 \times 10^{-4}$ m. We use a nonuniform radial grid in the vacuum region to resolve the structure of the antenna current, with approximately 25 radial grid points in the interval $[R - 6\Delta_r, R + 6\Delta_r]$.

¹R. W. Boswell, *Plasma Phys. Controlled Fusion* **26**, 1147 (1984).

²F. F. Chen, *Plasma Phys. Controlled Fusion* **33**, 339 (1991).

³R. W. Boswell and F. F. Chen, *IEEE Trans. Plasma Sci.* **25**, 1229 (1997).

⁴F. F. Chen and R. W. Boswell, *IEEE Trans. Plasma Sci.* **25**, 1245 (1997).

⁵F. F. Chen, *Phys. Plasmas* **4**, 3411 (1997).

⁶D. Arnush and F. F. Chen, *Phys. Plasmas* **5**, 1239 (1998).

⁷B. N. Breizman and A. V. Arefiev, *Phys. Rev. Lett.* **84**, 3863 (2000).

⁸M. I. Panevsky and R. D. Bengtson, *Phys. Plasmas* **11**, 4196 (2004).

⁹T. H. Stix, *Waves in Plasmas* (AIP, New York, 1992), p. 81.

¹⁰A. V. Gordeev and L. I. Rudakov, *Sov. Phys. JETP* **28**, 1226 (1968).

¹¹R. W. Boswell, *Phys. Lett.* **33**, 457 (1970).

¹²A. Komori, T. Shoji, K. Miyamoto, J. Kawai, and Y. Kawai, *Phys. Fluids B* **3**, 893 (1991).

¹³T. Shoji, Y. Sakawa, S. Nakazawa, K. Kadota, and T. Sato, *Plasma Sources Sci. Technol.* **2**, 5 (1993).

¹⁴P. A. Keiter, E. E. Scime, and M. M. Balkey, *Phys. Plasmas* **4**, 2741 (1997).

¹⁵A. W. Degeling, C. O. Jung, R. W. Boswell, and A. R. Ellingboe, *Phys. Plasmas* **3**, 2788 (1996).

¹⁶D. A. Schneider, G. G. Borg, and I. V. Kamenski, *Phys. Plasmas* **6**, 703 (1999).

¹⁷Y. Sakawa, M. Ohshima, Y. Ohta, and T. Shoji, *Phys. Plasmas* **11**, 311 (2004).

¹⁸A. W. Trivelpiece and R. W. Gould, *J. Appl. Phys.* **30**, 1784 (1959).

¹⁹K. P. Shamrai and V. B. Taranov, *Plasma Sources Sci. Technol.* **5**, 474 (1996).

²⁰S. Cho and J. Kwak, *Phys. Plasmas* **4**, 4167 (1997).

²¹F. F. Chen and D. D. Blackwell, *Phys. Rev. Lett.* **29**, 2677 (1999).

²²D. Arnush, *Phys. Plasmas* **7**, 3042 (2000).

²³S. Cho and M. A. Lieberman, *Phys. Plasmas* **10**, 882 (2003).

²⁴F. F. Chen, M. J. Hsieh, and M. Light, *Plasma Sources Sci. Technol.* **3**, 49 (1994).

²⁵Y. Mouzouris and J. E. Scherer, *Phys. Plasmas* **5**, 4253 (1998).

²⁶Th. Enk and M. Krämer, *Phys. Plasmas* **7**, 4308 (2000).

²⁷I. D. Sudit and F. F. Chen, *Plasma Sources Sci. Technol.* **3**, 162 (1994).

²⁸V. L. Ginzburg, *The Propagation of Electromagnetic Waves in Plasmas* (Pergamon, Oxford, 1964), p. 84.

²⁹E. F. Jaeger, D. B. Batchelor, H. Weitzner, and J. H. Wheaton, *Comput. Phys. Commun.* **40**, 33 (1986).

³⁰K. Yee, *IEEE Trans. Antennas Propag.* **AP-14**, 302 (1966).

³¹S. Balay, K. Buschelman, W. D. Gropp, D. Kaushik, M. G. Knepley, L. C. McInnes, B. F. Smith, and H. Zhang, *PETSc*, <http://www.mcs.anl.gov/petsc>, 2001.

³²P. Helander and D. J. Sigmar, *Collisional Transport in Magnetized Plasmas* (Cambridge University Press, Cambridge, UK, 2002), p. 5.

³³M. Hayashi, *Bibliography of Electron and Photon Cross Sections with Atoms and Molecules Published in the 20th Century (Argon)*, Report NIFS-DATA-72 (January 2003) (National Institute for Fusion Science, Toki, Japan), ISSN 0915-6364.

³⁴A. V. Arefiev, Ph.D. thesis, University of Texas at Austin, 2002.

³⁵D. G. Miljak and F. F. Chen, *Plasma Sources Sci. Technol.* **7**, 537 (1998).

³⁶M. Light, I. D. Sudit, F. F. Chen, and D. Arnush, *Phys. Plasmas* **2**, 4094 (1995).

³⁷*Handbook of Chemistry and Physics*, 41st ed., edited by C. D. Hodgman, S. M. Selby, and R. C. Weast (CRC, Cleveland, Ohio, 1960), p. 2528.